JOURNAL OF SPACECRAFT AND ROCKETS
Vol. 43, No. 2, March–April 2006

Experiments and Physical Modeling of Ultraviolet-Enhanced Contamination from Pure Contaminants

Alexandre Pereira* and Jean-François Roussel†
ONERA, 31055 Toulouse, France
Marc Van Eesbeek‡ and Olivier Schmeitzky§
ESA, 2200 AG Noordwijk ZH, The Netherlands
and
Delphine Faye¶
Centre National d'Etudes Spatiales, 31401 Toulouse, France

This work aims at understanding the synergistic effects of external contamination and solar ultraviolet (UV). A test facility and a physical model of major phenomena involved in UV-enhanced contamination were developed in collaboration among ONERA, ESA/European Space Research and Technology Center, and Centre National d'Etudes Spatiales. Deposition of contaminant models (pure chemical compounds) was performed on two different microbalances simultaneously with and without UV exposure, followed by a reemission phase and physicochemical analyses. In parallel, a multilayer physical model was developed and used to model experimental data. It takes into account physical phenomena such as adsorption and desorption and chemical mechanisms such as the creation of chromophores and bonds. Different regimes were studied, either at low temperature, resulting in deposit increase even without UV, or at high temperature, where an equilibrium is reached in the absence of UV. The model proved its ability to reproduce both regimes. Its number of free parameters was small enough to prove its predictive character. This work also showed the importance of the generation of oligomers and the existence of UV-induced bond scissions.

Nomenclature

A_D = prefactor of the Arrhenius law for the contaminant desorption from the quartz crystal microbalance (QCM)
A_f = prefactor of the Arrhenius law for the contaminant flux onto the QCM
A_P = prefactor for the vapor pressure Arrhenius law
C = contaminant in gas phase
C_{full} = surface concentration corresponding to a full monolayer
C_n = total surface concentration of the layer n
$C_n^{i,j,k}$ = surface concentration of molecules on layer n, with i chromophores, j bonds with other molecules, k with substrate
d = distance between the Knudsen cell orifice and the QCM
E_a^D = desorption activation energy
E_a^f = activation energy for the contaminant flux onto the QCM
F = view factor between the Knudsen cell orifice and the QCM
f_D = desorption flux (or evaporation), mass per surface and time unit
f_K = flow rate emitted from Knudsen cell, mass per time unit
f_{QCM} = arrival flux on QCM, mass per surface and time unit
H_s = heat of sublimation
H_v = heat of vaporization
I_n = photon flux received by layer n
k_C = kinetic constant of chromophore creation (cross section)
k_D^0 = desorption constant of simply condensed molecules
k_D^j = desorption constant of polymerized molecules
k_F = photofixation kinetic constant (cross section)
k_P = polymerization kinetic constant (cross section)
l = equivalent deposit thickness for vacuum ultraviolet (VUV) absorption (only aged molecules)
l_0 = VUV photon absorption coefficient
M = molar mass
m = total deposit mass
P = adsorption probability of an incoming contaminant
P_s = vapor pressure
q = volatility scaling factor (ratio of desorption constants of consecutive oligomers)
R = Boltzmann gas constant
r = radius of the Knudsen cell orifice
T = temperature
T_K = temperature of the Knudsen cell
T_{QCM} = temperature of the QCM box
T_{quartz} = temperature of the QCM quartz
T_{shroud} = temperature of the vacuum chamber shroud
V_A = adsorption rate
V_C = rate of chromophores creation
V_D = desorption rate
V_F = photofixation rate
V_P = polymerization rate
α = parameter of radiative thermal exchanges between the quartz and the shroud
α_s = solar absorptivity
β = parameter of thermal exchanges between the quartz and the QCM box
θ = angle between the Knudsen cell orifice normal and the orifice-to-QCM direction

Received 6 December 2004; revision received 29 August 2005; accepted for publication 10 September 2005.

*Ph.D. Student, Space Environment Department.
†Research Scientist, Space Environment Department.
‡Research Scientist, Materials Physics and Chemistry Section, Technical and Quality Management Directorate, European Space Research and Technology Center.
§Technician, Materials Physics and Chemistry Section, Technical and Quality Management Directorate, European Space Research and Technology Center.
¶Chemist, Propulsion, Pyrotechnic and Contamination Department.

τ_r = residence time
τ_0 = oscillation period (residence time for high T)
ψ = angle between the QCM normal and the QCM-to-Knudsen cell orifice direction

Introduction

MOLECULAR contamination of spacecraft surfaces is one of the most critical in-orbit problems contributing to material properties degradation. These effects can worsen with ultraviolet (UV) radiation because of photochemical reactions, inducing a fixation of the contaminants and a creation of chromophores in the deposited films.[1,2] These synergistic effects between the contamination and the space environment must thus be studied through theory and experiments, on ground and in flight.

A first step was performed at Aerospace Corp.[3–6] They experimented the slow growth of polymerized layers of pure contaminants under UV exposure. These data were well reproduced by a simple analytical model: in the absence of UV and at high enough temperature, an equilibrium between condensation and desorption happens and results in the presence of a fraction of a monolayer of adsorbed molecules, which in the presence of UV yields a constant accretion rate.[3–5] The study under progress aims at understanding and modeling a significantly broader range of situations and effects. It shall also address the regime of larger contaminant flux (condensation not balanced by reemission leading to growing condensate in the absence of UV), and transient effects. The capability to model transient effects may be needed to explain the larger contamination observed on the face of Satellite Pour l'Observation de la Terre (SPOT) sun-synchronous spacecraft, which is sunlit at eclipse exit.[2] Most physicochemical processes will be taken into account, such as the generation of free radicals inducing the creation of bonds between molecules and molecular fragments (polymerization), the creation of bonds between a molecule and the substrate (photofixation), and also the generation of chromophores in the deposited substance.

The experimental sections of this paper first describe the test setup and the contaminants. The physics and the numerical model of the contamination processes under UV exposure are presented next. The deposits obtained experimentally and numerically are then compared. Microscope and FTIR (Fourier transform infrared) analyses of contaminated substrates are finally reported.

Experimental

The ESTEC BA-3 system used for this experimental campaign is described in Fig. 1. Thanks to this system, we are able to simulate contaminant deposition under and without UV simultaneously. The setup comprises a Knudsen cell, two quartz crystal micro balances (QCM) facing this cell, which monitor the deposited contaminant, and a vacuum ultraviolet lamp (all of them in a vacuum chamber with refrigerated walls). A separating plate is placed between the two QCM in order to irradiate only one of them, simultaneously performing in this way both kinds of deposition: simple condensation and condensation with photodeposition.

The QCM used in these experiments have a frequency of 10 MHz and a mass sensitivity of 4.42×10^{-9} g · cm^{-2} · Hz^{-1}, and their electrodes were vapor-deposited with gold. The temperatures of the QCM are monitored by a thermal controller, thanks to a cooling bath of methanol connected to the QCM plate equipped with heaters and

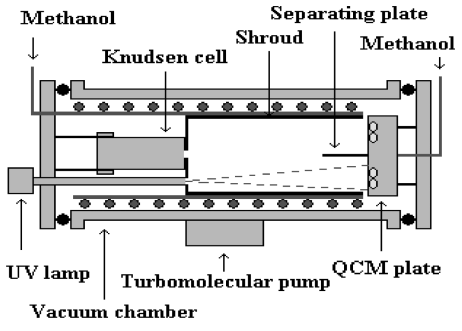

Fig. 1 BA-3 system.

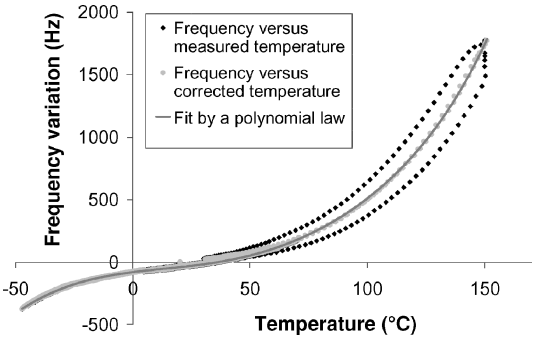

Fig. 2 Example of QCM calibration data (raw, corrected, and fitted).

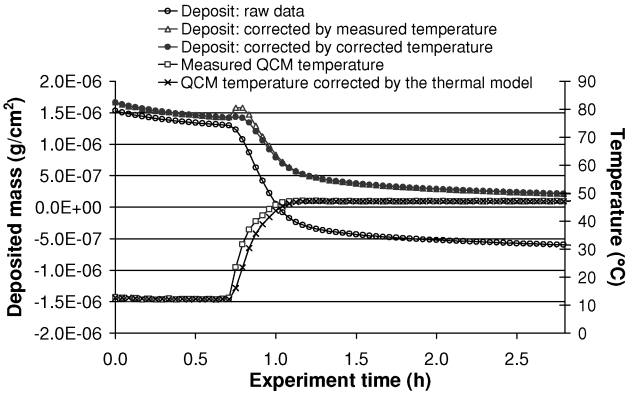

Fig. 3 Example of deposit (raw and corrected) and QCM temperature (measured and corrected).

thermal resistances (Pt-100). The data of each experiment are the QCM frequency transformed into mass deposit thickness, with a temperature correction taking into account the crystal frequency variations induced by crystal temperature changes. Before studying the deposition of contaminants, it is thus necessary to calibrate the frequency of the QCM as a function of its temperature. Typical calibration data are displayed in Fig. 2. The temperature of a clean QCM follows a double ramp (up, then down), during which its frequency varies. It also exhibits hysteresis, due to the thermal inertia of the quartz (the measured temperature is that of the QCM box, not of the quartz).

A first frequency correction was thus performed through a function of the quartz temperature (a polynomial). When corrected this way, a nonphysical mass variation due to the difference between the temperature measured on the QCM box and the real temperature of the quartz still was visible (see the "deposit corrected by measured temperature" curve of Fig. 3 around 0.8 h).

A second correction had thus to be applied to determine the real temperature of the quartz during the experiment. This correction was performed through a simple thermal model allowing us to take into account the inertia of the quartz. It is based on the thermal exchanges between the quartz and the QCM box and the vacuum chamber (the shroud indeed):

$$\frac{\mathrm{d}T_{\mathrm{Quartz}}}{\mathrm{d}t} = \alpha\left(T_{\mathrm{Shroud}}^4 - T_{\mathrm{Quartz}}^4\right) + \beta(T_{\mathrm{QCM}} - T_{\mathrm{Quartz}}) \qquad (1)$$

The thermal coupling of the quartz with the shroud is radiative, whereas it is both conductive and radiative with the QCM box (at temperature T_{QCM}), which led us to choose a linear coupling [second term in Eq. (1)], accounting for conductive or linearized radiative coupling. The α and β parameters were determined empirically. Typical values are $\alpha = 6 \times 10^{-3}$ K^{-3} · h^{-1} and $\beta = 1 \times 10^{-9}$ h^{-1}. Of course they could be obtained theoretically from emissivities, conductivities, heat capacity, geometry, and so forth, but it was not found to be more accurate to use an empirical fit. This thermal model gives good results, suppressing the calibration ramp hysteresis of Fig. 2 and the artifacts at temperature steps of experiments (Fig. 3).

The Knudsen cell is used to produce a molecular flux by effusion of our contaminant models. We have calibrated the molecular flux generated by the Knudsen cell by cooling the QCM to −50°C and measuring the deposit for various Knudsen cell temperatures. (The sticking coefficient is unity at −50°C for our contaminants.)

On the theoretical side, the mass flux onto the QCM, f_{QCM}, is related to the mass flow rate from the Knudsen cell, f_K, by means of the QCM-to-Knudsen cell orifice view factor F: $f_{\mathrm{QCM}} = f_K \times F$. F was derived from the solid angle from which the QCM is seen by the Knudsen cell orifice:

$$F = \frac{\cos\theta \cos\psi}{\pi d^2} \tag{2}$$

Then for simplicity's sake we assumed that the orifice transmission probability, or the fraction of molecules entering the upstream face of the orifice that pass through the downstream face, is unity for this configuration. For our geometry it leads to a difference of only about 4% from the classical American Society for Testing and Materials (ASTM) E1559-93 computation.[7] The arrival flux on QCM is thus given by

$$f_{\mathrm{QCM}} = P_s(T_K)\pi r^2 \sqrt{\frac{M}{2\pi RT_K}} \times \frac{\cos\theta \cos\psi}{\pi d^2} \tag{3}$$

the first term on the right-hand side of Eq. (3) being the flow rate f_K from the effusion cell.

The UV lamp used for all following experiments is a deuterium lamp. This lamp is placed outside the vacuum chamber, and the photon flux is directed through a waveguide to one of the QCM surfaces. In the rest of this paper, the QCM receiving this photon flux is called irradiated QCM, even when the lamp is switched off. In the range 114–180 nm, the integrated intensity, measured thanks to a gold detector, is about 2×10^{14} photons $\cdot$ cm$^{-2} \cdot$ s^{-1}, and so the acceleration is about 174 with respect to the solar flux (1.15×10^{12} photons $\cdot$ cm$^{-2} \cdot$ s^{-1}) (Ref. 8).

Contaminant Models

In the experiments presented here, we have used pure contaminants to know the outgassed molecules and to simplify the outgassing kinematics and the chemical reactions of polymerization. A few molecules were selected as being representative of general classes of compounds outgassed by spacecraft materials. The chosen contaminant models were di-iso-octylphtalate (DOP), very close to diethylhexylphtalate (DEHP), bisphenol-A, hexaphenylcyclotrisiloxane (HPTS), and octaphenylcyclotetrasiloxane (OPTS).

The flux of these contaminants onto the QCM needed to be known for arbitrary Knudsen cell temperature. They were first computed on a theoretical basis. The pure contaminant vapor pressure obeys an Arrhenius law, $P_s(T_K) = A_P \exp(-H_v/RT_K)$, with H_v the heat of vaporization of the contaminant (or sublimation for solids). The arrival fluxes were then obtained through Eq. (3). On the other hand, these fluxes were measured on the QCM and also exhibited Arrhenius behavior:

$$f_{\mathrm{QCM}} = A_f \exp\left(-E_a^f \big/ RT_K\right) \tag{4}$$

The experimental and theoretical Arrhenius parameters are compared in Table 1. (Vapor pressure data were found for DOP and bisphenol-A only.[9]) They exhibit a small discrepancy certainly due to the relatively narrow temperature range of this study.

Table 1 Arrhenius parameters for the incident contaminant flux onto QCM

	Experiment		Theory	
Material	E_a^F, kJ/mol	Ln(A_F), (A_F, g/cm^2/h)	E_a^F, kJ/mol	Ln(A_F), (A_F, g/cm^2/h)
DOP	109	25.2	118	26.7
Bisphenol-A	73	12.2	97	21.4
HPTS	198.5	42.8		
OPTS	173	32.8		

All of the tests performed consisted of two parts. In the first, we deposited the contaminants at constant QCM temperatures and with a constant flux of contaminants (constant Knudsen cell temperature). In the second, we stopped the deposition by cooling the Knudsen cell, and both QCM were heated to characterize the reemission kinetics of condensed and photofixed contaminants. The QCM heating was either performed by steps, or with the constant slope of a classical thermogravimetric analysis.

As these experiments rely on comparison of the deposits on the irradiated and nonirradiated QCM, it was necessary to check the equality of the arrival fluxes on both QCM, that is, the symmetry of the system. Two tests were performed for that purpose, with $T_K = 125$°C and 75°C respectively, and in both cases $T_{\mathrm{QCM}} = -50$°C, the UV lamp being switched off for symmetry. A small asymmetry of the deposits was found. Its constant value (10% at the first test and 9% at the second) confirmed the reproducibility of the data, the asymmetry of which was thus corrected.

Physics and Modeling

Physics of Simple Condensation

In the absence of UV irradiation, two different regimes can be achieved for the physical condensation of a pure compound. At cold receiver temperatures, the deposit increases continuously. In this case the emission law for thick deposits is the zero-order Langmuir law

$$f_D = P_s(T)\sqrt{M/2\pi RT} \tag{5}$$

For warmer receiver temperature (or smaller impinging flux) the deposit no longer increases after equilibrium between deposit and emission is reached. In that case, deposits are thin, on the order of a monolayer, and the desorption flux is usually modeled by a first-order desorption law following the residence time approach:

$$f_D = m/\tau_r = k_D^0 m \tag{6}$$

An example of both behaviors is reported in Fig. 4 for different QCM temperatures and the same impinging flux.

As will be seen, in a physical model the proper way to obtain both the zero-order and the first-order laws is to consider a multilayer model, as in Brunauer–Emmet–Teller (BET) theory for steady state.[10] At the microscopic level of an individual molecule the first-order law prevails, because a molecule has some probability of getting the energy to leave the condensed phase (given by an Arrhenius law again). This is, however, only true for molecules directly in contact with the gas phase (no other molecule on top of them), which leads to saturation, hence a zero-order law, when the first deposit layer is full.

Physics of Photoenhanced Contamination

In the presence of UV, chemical processes can occur while contaminant molecules are condensed (physisorbed). We shall distinguish the creation of bonds between molecules (which we call polymerization) and the creation of bonds between a molecule and the

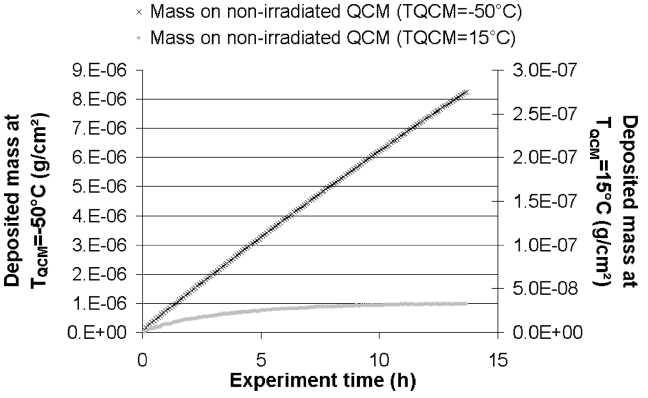

Fig. 4 Two regimes of condensation: increase of the deposit and equilibrium ($T_K = 60$°C, $f_{\mathrm{QCM}} = 6 \times 10^{-7}$ g $\cdot$ cm$^2 \cdot$ h^{-1}, DOP).

substrate (called photofixation). They usually result from the generation of radicals by ultraviolet. Concurrently, the molecular rearrangements induced by UV may present low-energy transitions, in the visible wavelength domain, that is, chromophores (such as conjugated π bonds). They affect the penetration of the photons through the layers of deposited contaminants, in the visible wavelengths (with effects on the mission), but also, and much more drastically, in the UV, which may reduce later UV-enhancement of contamination. In contrast, UV-induced scissions of bonds of macromolecules may result in the emission of molecular fragments.

For practical applications, the question to be addressed is then the following: which part of the molecules will be reemitted when the spacecraft or the QCM is heated up after deposition, and which part indeed became permanent, due to chemical bonding? This may be more complex than the simple accretion monolayer by monolayer. Since we wanted to address the regime of growing condensate (condensation not balanced by reemission in the absence of UV) and transient effects, it looked necessary to distinguish between the bonding with another condensed molecule and with the substrate (or with a fixed molecule). The dynamics of such molecules is very different in case of later heating up.

Modeling

As a consequence the model had to answer to the major requests to be multilayer and take into account many different mechanisms. They were thus represented by two physical reactions [Eqs. (7) and (8)] and three chemical reactions induced by UV [Eqs. (9–11)]:

$$\text{Adsorption } C \longrightarrow C_n^{0,0,0} \tag{7}$$

$$\text{Desorption } C_n^{i,j,0} \underset{k_D^j}{\longrightarrow} C \tag{8}$$

$$\text{Photofixation } C_n^{i,j,k} + h\nu \underset{k_F}{\longrightarrow} C_n^{i,j,k+1} \tag{9}$$

$$\text{Polymerization } C_n^{i,j,k} + h\nu \underset{k_P}{\longrightarrow} C_n^{i,j+1,k} \tag{10}$$

$$\text{Chromophores } C_n^{i,j,k} + h\nu \underset{k_C}{\longrightarrow} C_n^{i+1,j,k} \tag{11}$$

where $C_n^{i,j,k}$ represents the concentration of molecules adsorbed on layer n ($n = 1$ for the first layer directly on top of the substrate). In $C_n^{i,j,k}$ the indices i, j, and k represent the main effects of UV on these molecules (creation of bonds and optically active centers):

1) i is the aging number, that is, the number of chromophores per molecule (i is initially 0, then 1, sometimes more).

2) j is the polymerization number, that is, the number of bonds created between a molecule and others molecules (not fixed to the substrate).

3) k is the fixation number, that is, the number of bonds created between a molecule and the substrate or between a molecule and other already photofixed molecules.

For instance, $C_n^{2,1,0}$ is the concentration of molecules of the nth layer with two chromophores (per molecule), one bond with another molecule, and no bond with the substrate (or molecules themselves fixed to the substrate). $C_n^{0,0,0}$ represent the concentration of unmodified molecules on layer n. Of course the populations with small indices i, j, and k are the largest. The total concentration of a layer is

$$C_n = \sum_{i,j,k} C_n^{i,j,k} \tag{12}$$

with a maximum of C_{full}, corresponding to a full monolayer.

The deposition, Eq. (7), has the following rate for layer n (contributing to $C_n^{0,0,0}$ increase):

$$V_A = f_{\text{QCM}} P[(C_{n-1} - C_n)/C_{\text{full}}] \tag{13}$$

where $(C_{n-1} - C_n)/C_{\text{full}}$ represents the fraction of layer $n-1$ exposed to vacuum. The desorption rate of population $C_n^{i,j,k}$ [Eq. (8)] is given by

$$V_D\left(C_n^{i,j,k}\right) = \delta_{k,0} k_D^j [(C_n - C_{n+1})/C_n] C_n^{i,j,k} \tag{14}$$

where only nonfixed molecules can desorb ($k = 0$). The rate is again reduced by the "access-to-vacuum" ratio $(C_n - C_{n+1})/C_n$. The rates of photofixation, polymerization, and darkening of Eqs. (9–11) are eventually given by

$$V_F\left(C_n^{i,j,k}\right) = I_n k_F C_n^{i,j,k} \tag{15}$$

$$V_P\left(C_n^{i,j,k}\right) = I_n k_P C_n^{i,j,k} \tag{16}$$

$$V_C\left(C_n^{i,j,k}\right) = I_n k_C C_n^{i,j,k} \tag{17}$$

where I_n is the photon flux received by layer n. The generation of chromophores affects the penetration of the photons through the layers, resulting in smaller I_n for deeper layers. The model takes this phenomenon into account by using a photon absorption coefficient l_0, which results in a Beer–Lambert law

$$I_n \sim \exp(-l/l_0) \tag{18}$$

for a homogeneous deposit of thickness l, or for our deposit of equivalent deposit thickness l_0 (taking into account only aged molecules).

Before closing this section, the meaning of the index j, the polymerization number, must be discussed a little further. Because it represents the number of bonds of a contaminant molecule with other molecules, it might be thought that $C_n^{i,j,k}$ represents a concentration of polymers composed of $j+1$ contaminants ($j+1$ monomers). This idea is certainly too naive because in radical polymerization, radicals can be fragments of the initial monomer. A species of index j is thus indeed to be considered as a mixture of oligomers resulting from j radical polymerization steps. Its average weight increases with j, but by an amount smaller than the monomer weight.

Of course neither the masses nor the reemission time constants are known for these newly generated oligomers. We cannot hope for a detailed description of them. Moreover, we also wanted to avoid introducing too many "free" parameters into the model, which would loose its predictive character. So we simply assumed a geometric progression for the reemission kinetic constant of oligomers of increasing j in Eq. (14):

$$k_D^j = k_D^0 q^{-j}, \qquad k_D^0 = A_D e^{-E_a^D/KT} \tag{19}$$

where k_D^0 (for a monomer) follows a regular Arrhenius law and the desorption kinetic constants k_D^j (for heavier oligomers) are smaller by a factor of q for each next oligomer. This assumption has the merits of being simple and relatively realistic and introducing only one extra parameter q.

It can also be noticed in Eqs. (14) and (19) that we did not make a distinction between the first layer and the next ones. In studying the adsorption on a clean substrate, the first layer (or few layers) has to be handled differently because of its different affinity with the substrate than between contaminants themselves (cf., e.g., BET theory for the equilibrium with a gas phase below saturation pressure).[10] However, in space, contamination rarely happens on clean substrates, for example, as soon as a first layer is deposited. Moreover, because we were mostly interested in thick deposits, performing many extra experiments to determine data specific to the first layer did not seem necessary. So the same Eq. (19) is used throughout the deposit depth, with a single activation energy E_a^D, which is indeed the vaporization heat (moreover assumed identical for all oligomers for simplicity sake).

We did not make specific experiments to determine a very accurate value of C_{full}, the mass corresponding to a full layer, for the same reason. (It is not so important for thick deposit growth.) We rather used approximate values, assuming that layers are filled. The values were obtained from molecular weights and are, respectively, 26, 15, 39, and 53×10^{-8} g/cm^2 for DOP, bisphenol-A, HPTS, and OPTS (equivalent to site densities on the order of a few 10^{14} cm^{-2}). This

Table 2 Parameters for contaminant dynamics on the QCM quartz[a]

Material	E_a^D, kJ/mol	Ln(A_D), (A_D, h^{-1})	q	k_P	k_F	k_C
				$\times 10^{-20}$ cm^2		
DOP	118	53.3	2000	11	1.2	1
Bisphenol-A	97	45.9	100	38	9.6	1
HPTS	161	54.4	7	100	12	1
OPTS	170	52.6	7	50	7	1

[a]UV flux is 7.2×10^{17} cm$^{-2} \cdot h^{-1}$; incident flux data are in Table 1.

has the virtue of keeping a small number of free parameters in the model, but may be the origin of a reduced accuracy of the modeling of very small deposits on a clean QCM quartz (see later), and could perhaps be improved in the future.

The dynamics of each contaminant is thus finally governed by the following parameters: the three chemical reaction kinetic constants k_F, k_P, k_C (temperature-independent cross-sections indeed), the desorption parameters for all oligomers created, that the three parameters of Eq. (19), A_D, E_a^D, and q, hence a total of six parameters (cf. Table 2 for their values deduced from experiments in the next section). There are two extra parameters describing the incoming flux (Table 1), but they are indeed related to the desorption parameters, because this flux comes from Knudsen cell emissions. [Langmuir law (5) relates vapor pressure and evaporation from bulk condensate, which should be close to our desorption law equations (14) and (19) for at least a full layer, and it can indeed be checked that the corresponding activation energies E_a^f and E_a^D in Tables 1 and 2 are similar, typically up to 20%.]

Comparison of Experiments and Modeling

Our experiments were simulated with this multilayer model by adjusting the parameters. The impinging flux data (Table 1) were already known from initial outgassing experiments, and it remained to determine the next six unknown parameters: A_D, E_a^D, and q for desorption and k_F, k_P, and k_C for chemical reactions. On the data side, we had a full time evolution of the deposit, hence equivalent to many more than six scalar data. A good fit of the data will therefore confirm the correctness of the physics in the model (not necessarily the high accuracy of the parameters yet).

Without UV

We started modeling the simple physical condensation of molecules without UV. At cold enough QCM temperature (−50°C in our case), all contaminants are condensed. From these tests we derived the parameters of the impinging flux Arrhenius law of Eq. (4), reported in Table 1. Then the modeling of the reemission phase allowed us to obtain the desorption data, given in Table 2 (columns 2–4).

As an example, a comparison of an experiment with our modeling is reported in Fig. 5. The fit is good in both the deposition and reemission phases, as in most of the UV-off data. In this test the deposition ends at $t = 14.5$ h with the cooling of the Knudsen cell, and the reemission starts due to the heating of the QCM. Here the emission for thick deposits is the zero-order Langmuir law (5), as can (with difficulty) be seen from the constant slope at each reemission step. All molecules physically condensed on the QCM surface were reemitted

With UV, Cold QCM

For a cold QCM temperature, UV irradiation has no influence on the deposition rate, because all molecules striking the surface of the QCM are physically condensed. Such an example is reported in Fig. 6. In the reemission phase the UV effects, which were unobserved during the deposition phase, become apparent. The reemission is only partial because chemical bonds have been created between molecules (polymerization) or between molecules and the substrate (photofixation). In this example the mass reemitted from the irradiated QCM is about half of the total deposit. It is much more than a monolayer, which is not surprising because the deposition was

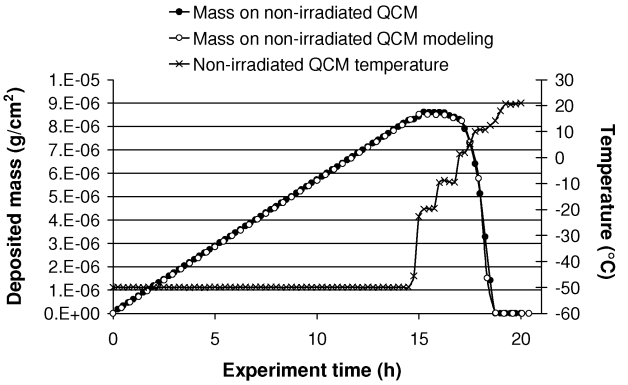

Fig. 5 DOP deposit, $T_K = 60°$C, UV off.

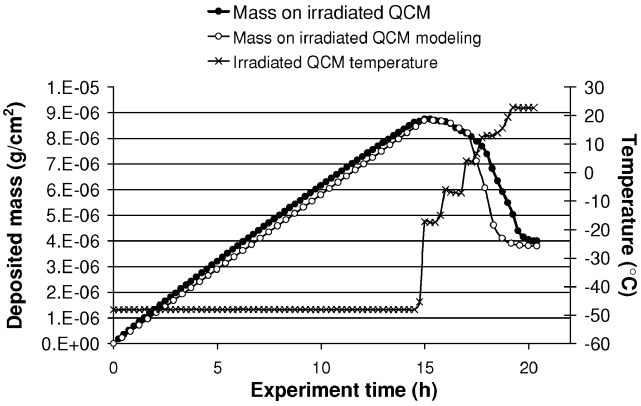

Fig. 6 DOP deposit, $T_K = 60°$C, UV on.

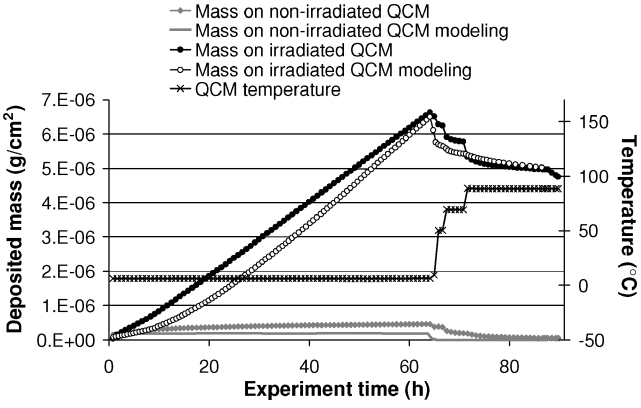

Fig. 7 Bisphenol-A deposit, $T_K = 80°$C, UV on again at $t = 88$ h (not modeled).

performed at low temperature. The reemitted fraction is quite variable depending on the deposition flux and duration, but correct fit modeling can be obtained in all situations (with the same set of six parameters for all experiments done with a single contaminant, we repeat).

With UV, Warmer QCM

Examples of experiments at a warmer receiver temperature are displayed in Figs. 7–9. Here, we represent the deposits on the irradiated and the nonirradiated QCMs (and their modeling). At such temperatures, reemission is not negligible and produces on the nonirradiated QCM either adsorption–desorption equilibrium with a deposit on the order of a monolayer (Figs. 7 and 9), or slow growth (Fig. 8). The modeling of the nonirradiated QCM deposit of Fig. 7 is not as good as for thicker ones, probably due to the approximate handling of the first deposit layer, as already mentioned.

In this case, the deposit on the irradiated QCM grows faster than that on the unexposed one. On the UV-exposed QCM the

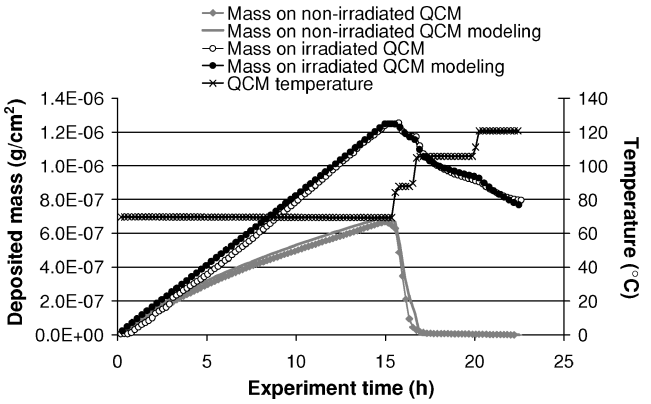

Fig. 8 HPTS deposit, $T_K = 130°C$.

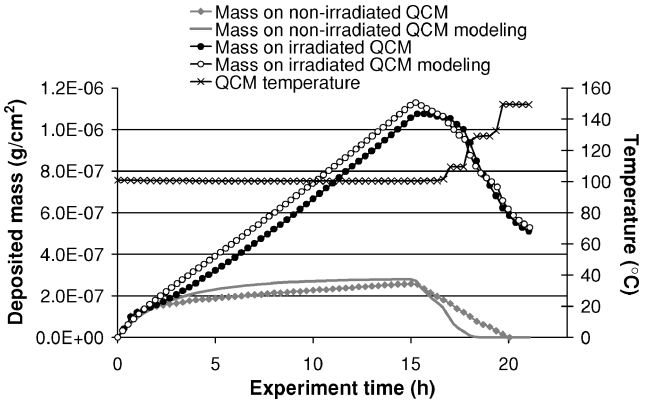

Fig. 9 OPTS deposit, $T_K = 160°C$.

condensation–desorption equilibrium also results in the presence of transiently physisorbed molecules, which can be photofixed and generate growth of the photofixed layers that can no longer be desorbed. As expected, at reemission only part of the deposit is evaporated.

A first interesting feature of the reemission phase is that reemission is still observed at rather warm temperatures, at which all primary contaminant is already reevaporated (see nonirradiated QCM). This is especially clear in Figs. 8 and 9. It can be explained only by the generation of larger molecules (oligomers) with smaller reemission constants. This oligomer generation was implemented in the model, leading to quite good reproduction of data.

A second point is that the reemitted amount is much larger than the deposit on the nonirradiated QCM, much larger than a monolayer. So the simple idea that the accretion mechanism is the progressive bonding of the physisorbed molecules (a fraction of a layer) residing on top of the growing chemically bonded deposit is too naive. As just discussed, there is at least a generation of larger molecules, too heavy to be emitted during the cold deposition phase, but outgassed later at warmer temperature. But there may also be molecules of the primary contaminant that remain trapped in the loose net of the reticulated deposit, which indeed generates more adsorption sites. In the model it would be modeled by the difficulty for the primary molecules of accessing from deep layers to vacuum (trapping in deepest layers). This hypothetical effect is, however, difficult to distinguish from the generation of oligomers just a little less volatile than the primary contaminant.

Discussion

Some other general aspects of these results deserve extra discussion. We first provide more detailed code outputs to show the reader how the code works. The population of each layer of the experiment of Fig. 6 is represented in Fig. 10. The deposition builds up simultaneously on many partial layers, the occupation of layer n following the occupation of layer $n-1$. It is somewhat similar to BET theory

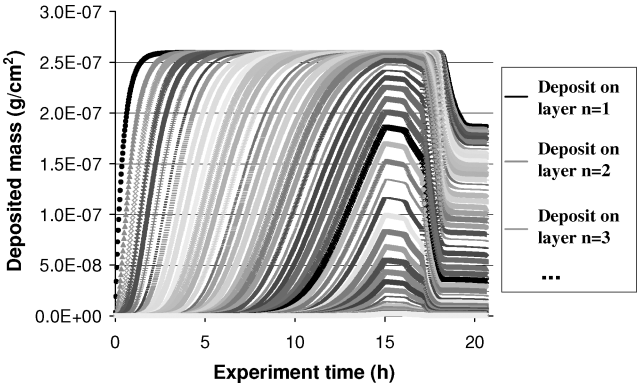

Fig. 10 Deposit mass depth profile on the irradiated QCM of Fig. 6.

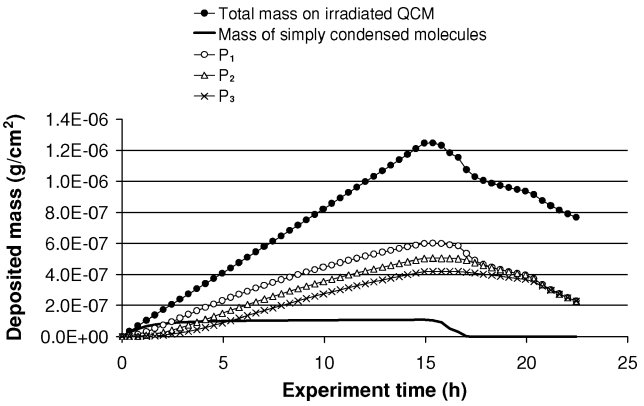

Fig. 11 Decomposition of the UV-enhanced deposit of Fig. 8: P_{j0} deposit contains molecules of polymerization number j larger than or equal to j_0, and not fixed ($\sum_{n,i,j\geq j_0} C_n^{i,j,0}$), whereas simply condensed molecules are $\sum_{n,i} C_n^{i,0,0}$.

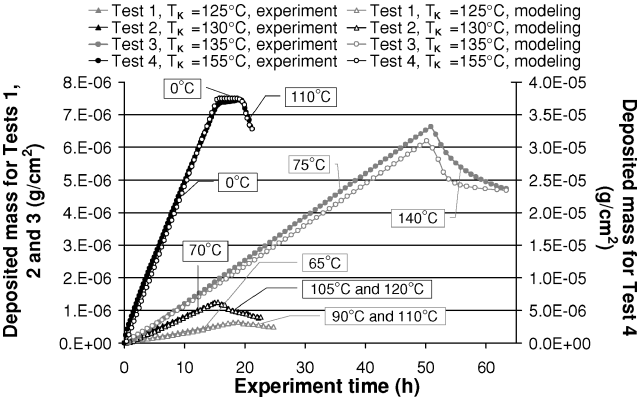

Fig. 12 Compilation of all experiments with HPTS. Last curve is on the second axis.

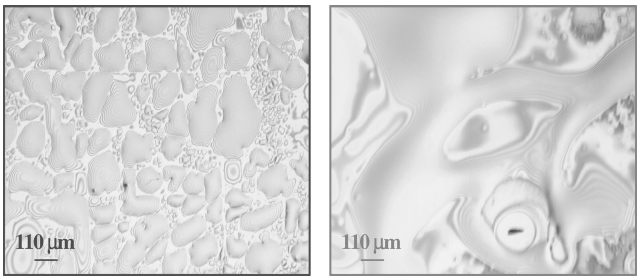

a) b)

Fig. 13 OSR contaminated with DOP: a) simple condensation and b) photodeposition.

for equilibrium theory. Rather orthogonally, Fig. 11 shows how the deposit of Fig. 8 is distributed between molecules of different polymerization number j. The oligomers with $j = 1$ are desorbed in the $t = 15$–17-h timeframe, and then the ones with $j = 2$ in the 16–20-h timeframe and the ones with $j = 3$ are only partially reemitted after $t = 20$ h. The difference between the P_1 curve and the total deposit curve is the sum of two populations: primary contaminants (those of the fifth curve), which are reemitted in the $t = 15$–17-h timeframe, and fixed molecules ($k > 0$), which would not be evaporated at any temperature (hence the constant P_1-to-total difference in the 17–23-h timeframe).

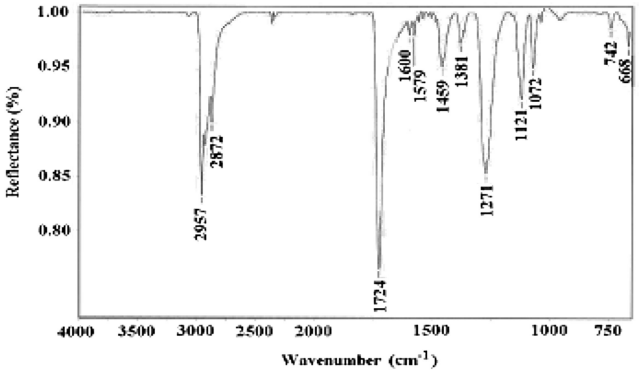

Fig. 14 FTIR spectrum of DOP deposited on an OSR without UV exposure.

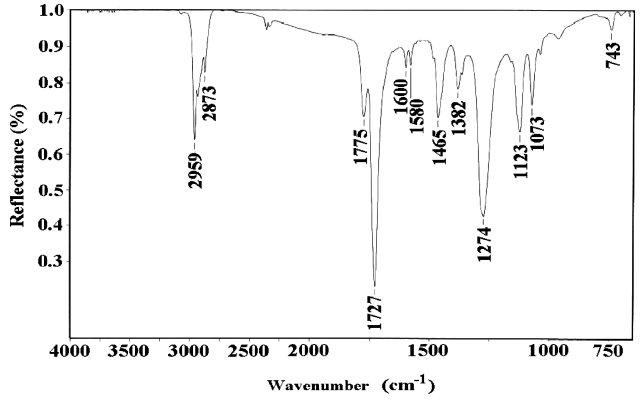

Fig. 15 FTIR spectrum of UV-deposited DOP on OSR.

Figure 12 is a compilation of all the experiments done with a single contaminant, HPTS, showing that we really fit a lot of data with few parameters. Here, we only had the six free parameters for HPTS (cf. Table 2) to fit the four curves of this figure (much more data), which supports the validity our physical assumptions.

The values of the volatility scaling parameter q also deserve a discussion. They are very different, ranging from 7 to 2000 for different contaminants (see Table 2). This may indicate that HPTS and OPTS, with $q = 7$, produce oligomers slightly heavier than themselves (e.g., one extra diphenylsiloxane group), whereas bisphenol-A and DEHP produce much heavier oligomers (relative to the monomer) by the bonding of a large fraction of the monomer. For example, adding half of a monomer to another one looks consistent with the structure of these molecules. We want as yet to remain very cautious with these considerations, and this kind of assumption would need to be confirmed by chromatography or mass spectrometry analyses, which could not be performed in the frame of this study. Moreover, the values of q are rather inaccurate, as it can be inferred from the fit of the reemission phases, which usually exhibit a good prediction of the reemitted amount (good k_F, k_P), but a poorer fit of the dynamics [less accurate q, or too simple geometric scaling of Eq. (19)].

We also investigated the scission of bonds by UV. In regular experiments, UV is turned off during the reemission phase. However, in Fig. 7, the UV lamp was turned on at the very end of the test, resulting in a clear increase of the mass loss rate. The only explanation is the UV-induced bond scission of macromolecules, producing smaller volatile molecular fragments. The emission rate was measured as around $1 \times 10^{-7}\ \mathrm{g \cdot cm^2 \cdot h^{-1}}$, but better characterization is still needed. It should in particular be dependent of the existing deposit thickness, due to scissions deep within the deposit. This extra phenomenon should in the future be included in the model. It may also be the origin of the tiny concavity (deposition rate decrease) in Fig. 6, which does not exist for the very linear deposit on the unexposed QCM (not represented, for clarity, because it is almost identical to the one with UV).

Concerning the vacuum ultraviolet (VUV) absorption coefficient of the studied contaminants [Eq. (18)], we used results from the Aerospace Corporation.[6] They measured the absorption coefficient in the range 250–700 nm for already aged molecules of bisphenol-A, diethylhexylphtalate, and tetramethyltetraphenyltrisiloxane, and the

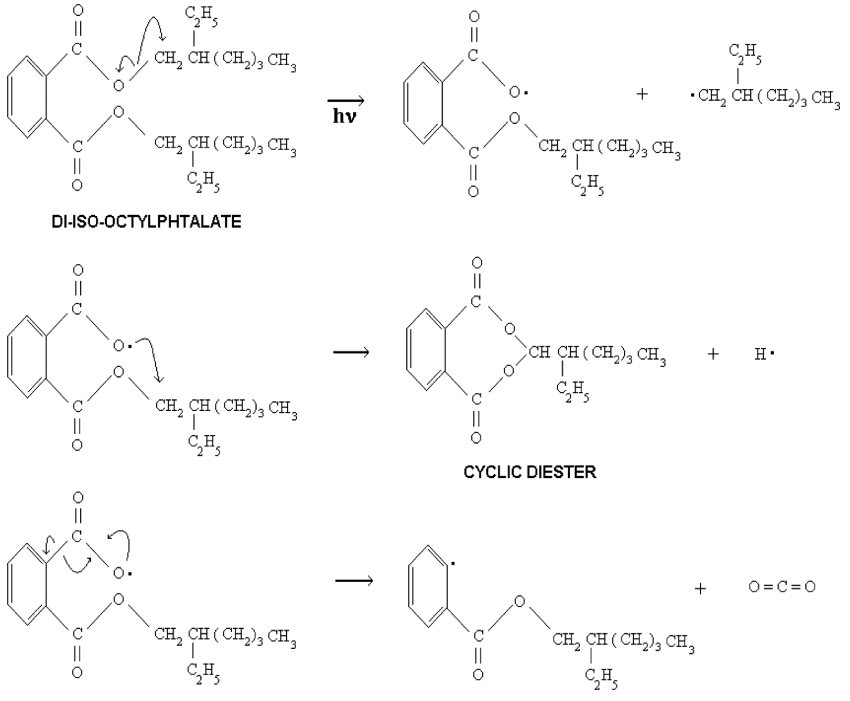

Fig. 16 Polymerization of DOP (di-iso-octylphtalate) and DEHP (diethylhexylphtalate).

extrapolation to 200 nm gives an absorption coefficient around 100 μm^{-1}, which we used for l_0. Further VUV absorption measurements should be done in future to improve this.

Chemical and Optical Characterization of Samples

We placed an OSR (optical solar reflector) beside the QCMs to characterize the physical structures of the photodeposited film and the simply condensed film. Optical microscopy photographs of OSR samples contaminated with DOP are displayed in Fig. 13. The first striking observation is that the global morphology of the two contaminated samples is totally different. In the case of simple physical condensation of molecules, the deposit shows a typical shape of droplets resulting from superficial tensions of the liquid contaminant. Concerning the irradiated OSR, the picture is more consistent with a polymerized network (or polymeric film).

FTIR spectroscopy analyses were also performed to determine which kinds of molecules are created by the polymerization of the DOP. The most characteristic absorption bands of pure DOP molecules can be observed in Fig. 14 (nonirradiated DOP): C–H stretching vibrations (2872 and 2957 cm^{-1}), aromatic C–H (tiny band at 3050 cm^{-1}), ester function (1724 cm^{-1}), C=C aromatic bond (1579–1600 cm^{-1} doublet), CH_2 and CH_3 rocking deformations (1381 and 1459 cm^{-1}), C–O (1271, 1121, and 1072 cm^{-1}), and 1,2-disubstitued benzenic cycle (742 and 668 cm^{-1}). In Fig. 15 the FTIR spectrum of the DOP deposited under UV exposure exhibits a similar spectrum, with a few changes. The band associated with the ester function is split into two neighbor bands at 1775 and 1727 cm^{-1}. This is the sign of the creation of a cyclic diester.[11] As shown in Fig. 16, a cyclic diester can be created from the DOP by a succession of radical reactions. The reactions of Fig. 16 of course have to be considered as a possible path, but are clearly not exhaustive, and other radicals can be created as well. The emergence of a small continuum in the range 2500–1800 cm^{-1} (or rather 2500–900 cm^{-1}) can be due simply to a larger signal on the irradiated sample (more deposit). The detailed interpretation of the FTIR spectra of the other contaminant deposits was rather difficult because of the smaller deposit thickness. Other analysis techniques should be used in future.

Conclusions

This paper presents a comparison between a physical modeling and an experimental study of phenomena occurring during the photodeposition of pure contaminants. Our multilayer model correctly reproduces experiments involving a broad range of regimes and effects: physical condensation leading to deposit growth or adsorption–desorption equilibrium, accretion in the presence of UV in any of these regimes through polymerization or fixation to the substrate, and finally the reemission of primary contaminants or newly created oligomers. FTIR spectroscopy analyses also provided interesting information about the products obtained from DOP under UV irradiation.

Although taking into account many phenomena, the model contains few parameters for each contaminant (Table 2), three for physical adsorption and desorption, and three cross sections for UV-induced chemical reactions. We did not focus on very accurate determination of these parameters, but rather on testing a broad range of situations (different temperature and flux profiles, different contaminants) to make sure that the physics taken into account in the model was describing reality. So the major outcome of this study is not an accurate parameter set, even though the parameters give correct estimates, but the validation of the physical phenomena involved in the UV–contamination synergies.

This opens many different perspectives for further studies. On the academic side, better determination of the chemical reactions and products induced by UV can be attempted. The model can also be refined, taking the chemical reactions into account more finely, adding the chain scissions, or determining the model parameters more accurately. This may involve many more experiments. On the practical side, real contaminant sources of course have to be considered, that is, materials outgassing many different molecules. In principle this can be handled by summing the contributions of all of them (if the physics is linear). Even then, there may yet remain a long way to the goal, because the numbers of species and parameters may become too large to be determined experimentally and implemented in engineering code.

References

[1]Tribble, A. C., and Haffner, J. W., "Estimates of Photochemically Deposited Contamination on the GPS Satellites," *Journal of Spacecraft and Rockets*, Vol. 28, No. 2, 1991, pp. 222–228.

[2]Roussel, J.-F., Alet, I., Faye, D., and Pereira, A., "The Effect of Space Environment on Spacecraft Thermal Control Coatings on Sun-Synchronous Orbits," *Journal of Spacecraft and Rockets* (to be published).

[3]Stewart, T. B., Arnold, G. S., Hall, D. F., and Marten, H. D., "Absolute Rates of Vacuum-Ultraviolet Photochemical Deposition of Organic Films," *Journal of Physical Chemistry*, Vol. 93, No. 6, 1989, pp. 2392–2400.

[4]Stewart, T. B., Arnold, G. S., Hall, D. F., Marvin, D. C., Hwang, W. C., Owl, R. C., and Marten, H. D., "Photochemical Spacecraft Self-Contamination: Laboratory Results and Systems Impacts," *Journal of Spacecraft*, Vol. 26, No. 5, 1989, pp. 358–367.

[5]Arnold, G. S., Owl, R. C., and Hall, D. F., "Optical Effects of Photo-Chemically Deposited Contaminant Films," *Proceedings of SPIE*, Vol. 1329, July 1990, pp. 255–265.

[6]Arnold, G. S., and Luey, K., "Photo-Chemically Deposited Contaminant Film Effects," *Proceedings of SPIE*, Vol. 2864, Aug. 1996, pp. 269–284.

[7]"Standard Test Method For Contamination Outgassing Characteristics of Spacecraft Materials," American Society for Testing and Materials, ASTM E1559-93, Oct. 1993.

[8]Jursa, A. S., *Handbook of Geophysics and the Space Environment*, U.S. Air Force Geophysics Lab., Hanscom, MA, 1985, pp. 4–10.

[9]Weast, R. C., *Handbook of Chemistry and Physics*, 57th ed., CRC Press, Boca Raton, FL, 1977, pp. D191–D208.

[10]Brunauer, S., Emmet, P. H., and Teller, E., "Adsorption of Gases in Multimolecular Layers," *Journal of the American Chemical Society*, Vol. 60, 1938, pp. 309–319.

[11]Pouchert, C. J., *The Aldrich Library of FT-IR Spectra*, Vols. 1 and 2, Aldrich Chemical Co., Milwaukee, WI, 1985.

J. Kleiman
Guest Editor